Available online at www.eccomasproceedia.org
Eccomas Proceedia SMART (2023) 498-506

ECCOMAS
Proceedia

X ECCOMAS Thematic Conference on Smart Structures and Materials
SMART 2023
D.A. Saravanos, A. Benjeddou, N. Chrysochoidis and T. Theodosiou (Eds)

IMPLEMENTATION OF MULTI-TYPE SENSOR PLACEMENT STRATEGY FOR LARGE-SCALE ENGINEERING STRUCTURES

BARTŁOMIEJ BŁACHOWSKI*, ANDRZEJ ŚWIERCZ*, PIOTR OLASZEK†, ŁUKASZ JANKOWSKI*

*Institute of Fundamental Technological Research, Polish Academy of Sciences
Pawińskiego 5B, Warsaw 02-106, Poland

†Road and Bridge Research Institute, Instytutowa 1, Warsaw 03-302, Poland

Abstract. The methodology for optimal single-type sensor placement has been extensively discussed in the literature. However, little attention has been devoted to the distribution of multi-type sensors. The application to large structures, such as bridges or towers, poses a significant challenge. Some responses, for example, the displacements of a bridge over a river, cannot be easily measured directly. Consequently, indirect techniques can be employed to estimate the deflections of such structures. In this contribution, a Kalman filter-based algorithm is presented to address this sensor placement problem. The effectiveness of the proposed method is numerically demonstrated using the example of an actual tied-arch bridge.

Key words: sensors, optimal sensor placement, Kalman filter, reduced order model, arch bridge

1 INTRODUCTION

One of the first studies targeting optimal placement of sensors is presented in [1]. In this study, the authors utilized a mass-lumped beam that has an unknown shear stiffness. To minimize the uncertainties of the related stiffness parameters, the singular value decomposition of the displacement sensitivity matrix was applied. More elaborate analyses can be found in [2], which employ the Fisher Information Matrix (FIM). The article [3] focuses on two sensor placement tests along a simply supported beam under random load. A different approach is introduced in [4], called Effective Independence (EFI), with an illustrative application to a space structure. This method aims to iteratively maximize the determinant of the FIM. Based on the mode shapes, the location contributing the least to the rank of the FIM is deleted from the set of candidate sensor locations. A version of the method that considers measurement noise is described in [5]. The EFI has proven to be an important concept and has been used in several further works, such as [6, 7, 8] and in the approach presented in [9] which employed convex relaxation (CR) for computational efficiency. In [10], the authors presented a probabilistic concept rooted in the Bayesian framework. The goal was to find the sensors locations that result in the least estimation uncertainty of the identified structural parameters. A genetic algorithm

Peer-review under responsibility of the organizing committee of SMART 2023.
doi: 10.7712/150123.9804.445332

was applied for optimization, system identification, and detection of damage. An extension of this approach is presented in [11], where the sensors are sequentially placed one by one in the position that yields the greatest entropy reduction. Reference [12] provides a comprehensive review of Bayesian method applications to model updating of dynamical systems. The kriging method is utilized in [13] to state the objective function based on the response estimation error. The best placements of the available sensors are found using an algorithm that combines genetic and gradient procedures.

Measurements of displacement can be conducted using various methods, among which direct reference-based techniques such as linear variable differential transducers, laser Doppler vibrometers, and computer vision-based systems [14] are most popular. Additionally, combined [15] and indirect methods [16] are often employed. This work addresses the problem of optimal sensors placement for displacement evaluation of a railway bridge using two types of inertial sensors.

2 THE RAILWAY ARCH BRIDGE

To evaluate the sensor selection procedure, a railway arch bridge located in central Poland was chosen as the test subject. It is a single-track structure, which primarily serves passenger trains traveling at speeds of up to 200 km/h, inducing predominantly vertical vibrations. A full order numerical model was developed using the Abaqus software package. A general view of the model is presented in Fig. 1a. A modal analysis was then conducted, resulting in the full mode shapes matrix $\boldsymbol{\Phi}_{\mathrm{F}}$. From this matrix, few primary (dominant) mode shapes, denoted as $\boldsymbol{\Phi}_{\mathrm{FP}}$, were extracted in accordance with the following formula:

$$\mathbf{q}_{\mathrm{F}}(t) = \boldsymbol{\Phi}_{\mathrm{F}}\,\boldsymbol{\eta}_{\mathrm{F}}(t) = \begin{bmatrix} \boldsymbol{\Phi}_{\mathrm{FP}} & \boldsymbol{\Phi}_{\mathrm{FS}} \end{bmatrix} \begin{bmatrix} \boldsymbol{\eta}_{\mathrm{P}}(t) \\ \boldsymbol{\eta}_{\mathrm{S}}(t) \end{bmatrix} \approx \boldsymbol{\Phi}_{\mathrm{FP}}\,\boldsymbol{\eta}_{\mathrm{P}}(t), \tag{1}$$

where the vector $\mathbf{q}_{\mathrm{F}}$ represents generalized displacements, while $\boldsymbol{\eta}_{\mathrm{P}}$ and $\boldsymbol{\eta}_{\mathrm{S}}$ denote the modal coordinates for primary and secondary mode shapes, respectively. The term $\boldsymbol{\Phi}_{\mathrm{FS}}\,\boldsymbol{\eta}_{\mathrm{S}}(t)$ does not significantly contribute to the structural response $\mathbf{q}_{\mathrm{F}}(t)$, and it is neglected in the following derivations.

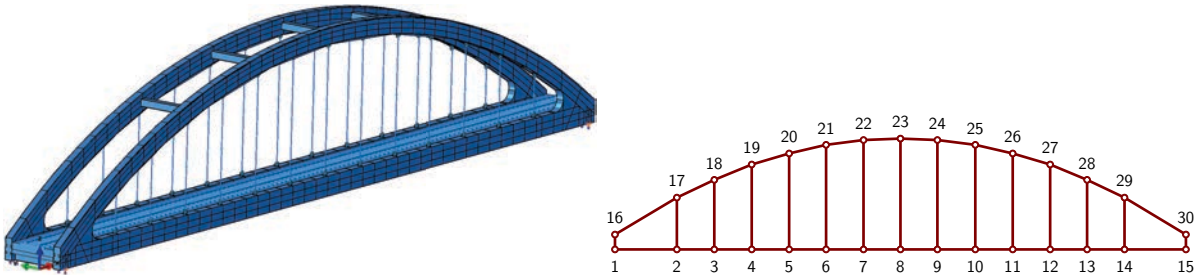

(a) Fine finite model (3D). (b) Coarse finite model (2D).

Figure 1: Numerical models of the single track railway bridge.

Processing the full-order model requires considerable computational resources; hence, a reduced-order model, as illustrated in Fig. 1b, with a coarser discretization can be efficiently employed. To obtain the generalized displacements, $\mathbf{q}_\mathrm{R}$, and the mode shapes, $\mathbf{\Phi}_\mathrm{R}$, from the full-order model, the selection matrix $\mathbf{L}$ can be utilized:

$$\mathbf{q}_\mathrm{R}(t) = \mathbf{L}\,\mathbf{q}_\mathrm{F}(t), \qquad \mathbf{\Phi}_\mathrm{R} = \mathbf{L}\,\mathbf{\Phi}_\mathrm{FP}. \tag{2}$$

Subsequently, the equation of motion for the reduced-order model can be expressed as:

$$\ddot{\boldsymbol{\eta}}_\mathrm{P}(t) + 2\boldsymbol{Z\Omega}\,\dot{\boldsymbol{\eta}}_\mathrm{P}(t) + \mathbf{\Omega}^2\boldsymbol{\eta}_\mathrm{P}(t) = \mathbf{\Phi}_\mathrm{R}^\mathrm{T}\mathbf{B}_\mathrm{R}\mathbf{u}_\mathrm{R}(t), \tag{3}$$

where the diagonal matrices $\mathbf{Z}$ and $\mathbf{\Omega}$ contain the viscous damping ratios and natural frequencies, respectively. The matrix $\mathbf{B}_\mathrm{R}$ arranges the loads over the DOFs of the reduced-order model, and $\mathbf{u}_\mathrm{R}$ is the load exerted by the train. The state-space representation of the dynamic system can be written with the observation vector $\mathbf{y}(t)$:

$$\begin{cases} \dot{\mathbf{z}}(t) = \mathbf{A}_\mathrm{c}\,\mathbf{z}(t) + \mathbf{B}_\mathrm{c}\,\mathbf{u}(t) + \mathbf{w}(t), & \text{(4a)} \\ \mathbf{y}(t) = \mathbf{C}\,\mathbf{z}(t) + \mathbf{D}\,\mathbf{u}(t) + \mathbf{v}(t), & \text{(4b)} \end{cases}$$

where $\mathbf{w}(t)$ and $\mathbf{v}(t)$ represent the unknown disturbances of the process and the measurement noise, respectively. The state and input matrices are represented by $\mathbf{A}_\mathrm{c} = \begin{bmatrix} \mathbf{0} & \mathbf{I} \\ -\mathbf{\Omega}^2 & -2\mathbf{Z\Omega} \end{bmatrix}$ and $\mathbf{B}_\mathrm{c} = \begin{bmatrix} \mathbf{0} & \mathbf{\Phi}_\mathrm{R}^\mathrm{T}\mathbf{B}_\mathrm{R} \end{bmatrix}^\mathrm{T}$. The output matrix $\mathbf{C}$ and the direct transmission matrix $\mathbf{D}$ are defined as:

$$\mathbf{C} = \begin{bmatrix} \mathbf{C}_\mathrm{d}\mathbf{\Phi}_\mathrm{R} & \mathbf{0} \\ \mathbf{C}_\mathrm{i}\mathbf{\Phi}_\mathrm{R} & \mathbf{0} \\ -\mathbf{C}_\mathrm{a}\mathbf{\Phi}_\mathrm{R}\,\mathbf{\Omega}^2 & -\mathbf{2C}_\mathrm{a}\mathbf{\Phi}_\mathrm{R}\mathbf{Z}\,\mathbf{\Omega} \end{bmatrix} \quad \text{and} \quad \mathbf{D} = \begin{bmatrix} \mathbf{0} \\ \mathbf{0} \\ \mathbf{C}_\mathrm{a}\mathbf{\Phi}_\mathrm{R}\mathbf{\Phi}_\mathrm{R}^\mathrm{T}\mathbf{B}_\mathrm{R} \end{bmatrix}. \tag{5}$$

In Eq. (4b) the observation vector $\mathbf{y}(t)$ is arranged by displacement sensors, inclinometers, and accelerometers, where the matrices $\mathbf{C}_\mathrm{d}$, $\mathbf{C}_\mathrm{i}$, and $\mathbf{C}_\mathrm{a}$ in Eq. (5) are the output submatrices for the aforementioned sensors.

3 SENSOR SELECTION PROCEDURE BASED ON KALMAN FILTER

For practical applications involving real measurements, the discrete-time state-space representation with zero-order hold (ZOH) is used instead of the continuous-time representation. For this purpose, Eqs. (4) are rewritten as:

$$\begin{cases} \mathbf{z}_{k+1} = \mathbf{A}\,\mathbf{z}_k + \mathbf{B}\mathbf{u}_k + \mathbf{w}_k, & \text{(6a)} \\ \mathbf{y}_k = \mathbf{C}\,\mathbf{z}_k + \mathbf{D}\mathbf{u}_k + \mathbf{v}_k, & \text{(6b)} \end{cases}$$

In these equations, $\mathbf{z}_{k+1} = \mathbf{z}(k\Delta t + \Delta t)$ and $\mathbf{z}_k = \mathbf{z}(k\Delta t)$ denote the discrete-time state vectors computed at the $(k+1)$st and kth time step, respectively, where Δt represents the time step.

The state and input matrices formulated in discrete time, $\mathbf{A}$ and $\mathbf{B}$, depend on the corresponding continuous-time matrices stated in Eq. (5) as follows:

$$\mathbf{A} = e^{\mathbf{A}_\mathrm{c}\Delta t}, \qquad \mathbf{B} = \mathbf{A}_\mathrm{c}^{-1}\left(e^{\mathbf{A}_\mathrm{c}\Delta t} - \mathbf{I}\right)\mathbf{B}_\mathrm{c}.$$

The observation vector $\mathbf{y}_k$ has components that they differ by orders of magnitude. To avoid numerical problems, the vector is normalized using a diagonal matrix $\mathbf{S}$ in the following way:

$$\widetilde{\mathbf{y}}_k = \mathbf{S}\mathbf{y}_k = \mathbf{S}\mathbf{C}\mathbf{z}_k + \mathbf{S}\mathbf{D}\mathbf{u}_k = \widetilde{\mathbf{C}}\mathbf{z}_k + \widetilde{\mathbf{D}}\mathbf{u}_k, \tag{7}$$

where the diagonal of $\mathbf{S}$ is defined by the reciprocals of standard deviations, σ_d^{-1}, σ_i^{-1}, and σ_a^{-1}, of the measurement noise corresponding to the displacement sensors, inclinometers, and accelerometers.

The Kalman filter estimates the current state in an iterative fashion. The algorithm is listed in Fig. 2. Each iteration consists of two steps: (a) the time update, which is based on the information from the previous time step, and (b) the measurement update based on the measurements performed in the current time step. As a result, an estimate of the full state vector $\hat{\mathbf{z}}_k^+$ and its covariance matrix $\mathbf{P}_k$ are computed in each time step. The matrix $\mathbf{P}_k$ tends to converge

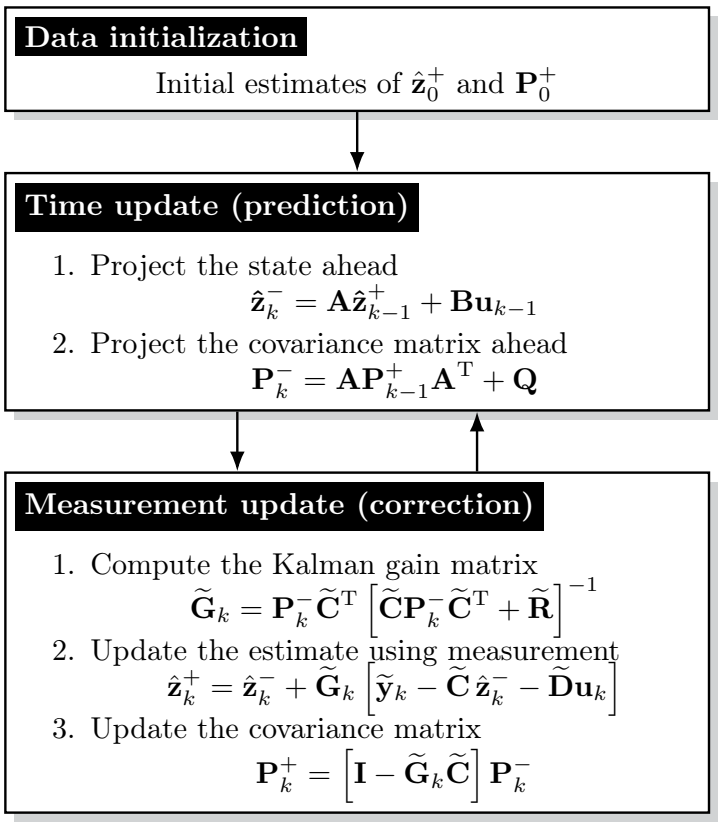

Figure 2: Kalman filter algorithm.

asymptotically to a certain fixed matrix $\mathbf{P}$. Finally, the covariance matrix $\mathbf{F}$ of the estimated unmeasured target responses of interest is given by

$$\mathbf{F} = \widetilde{\mathbf{C}}^{\mathrm{e}}\mathbf{P}\left(\widetilde{\mathbf{C}}^{\mathrm{e}}\right)^{\mathrm{T}}. \tag{8}$$

The optimal sensor configuration is obtained iteratively, with sensors deleted one at a time from the candidate sensor set in each iteration. The covariance matrix $\mathbf{F}$ is determined for the current candidate sensor set and used to assess the associated estimation error. The estimation error can be defined in different ways; however, in this work, two measures are considered: one based on the Frobenius norm $\epsilon^{\mathrm{F}} = \|\mathbf{F}\|_{\mathrm{F}}$ and one utilizing the mean diagonal of the covariance matrix $\mathbf{F}$, i.e., $\epsilon = \mathrm{mean}(\mathrm{diag}(\mathbf{F}))$. The iterative sensor removal process is performed in the two following ways:

1. using the greedy algorithm, where the testing covariance matrices $\mathbf{F}_j$ and the corresponding estimation error (ϵ_j^{F} or ϵ_j) are computed for the candidate sensor set with the jth sensor deleted. This is repeated for all sensors j, and finally, the sensor is removed whose removal generates the best estimation error. This is the reference approach proposed earlier in [17, 18].
2. based on the magnitude of the rows of the cross-covariance matrix $\mathbf{F}^{\mathrm{C}} = \widetilde{\mathbf{C}}\mathbf{P}\left(\widetilde{\mathbf{C}}^{\mathrm{e}}\right)^{\mathrm{T}}$. The row with the minimum magnitude corresponds to the deleted sensor. Thereafter, both estimation error measures ($\boldsymbol{\epsilon}^{\mathrm{F}}$ and $\boldsymbol{\epsilon}$) are computed to assess the error.

The greedy algorithm requires a significantly larger computational effort compared to the second approach. The iteration process is terminated when either the desired number of sensor is achieved or a limit estimation error is reached.

4 NUMERICAL EXAMPLE

To perform numerical tests of sensor placement, consider the arch bridge discussed in Section 2. The bridge is loaded by a 24-axle passenger train travelling at a speed of 160 km/h. The candidate sensor set includes inclinometers and accelerometers at all nodes of the reduced order model, as shown in Fig. 3. Horizontal and vertical displacements were selected for evaluating structural vibrations as the target response location set. Six primary modes are used to approximate the structural vibrations, and it is assumed that six sensors are to be placed over the structure.

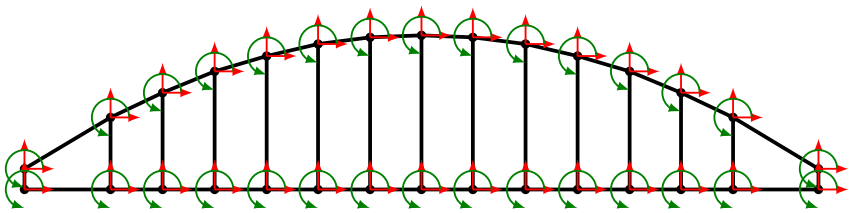

Figure 3: Candidate sensor set: inclinometers (green colored) and accelerometers (in horizontal and vertical directions, red colored).

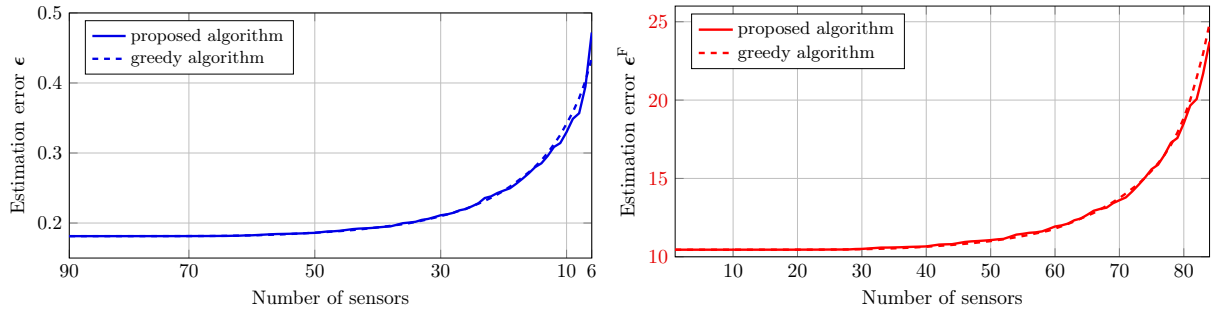

(a) (b)

Figure 4: Estimation errors during iterations using (a) mean diagonal and (b) Frobenius norm of the covariance matrix.

Table 1: Estimation errors in the last (84th) iterations.

proposed algorithm		greedy algorithm	
ϵ_{84}	$\epsilon^{\mathrm{F}}_{84}$	ϵ_{84}	$\epsilon^{\mathrm{F}}_{84}$
0.472	23.734	0.436	24.889

For both algorithms, the estimation errors (ϵ_i^{F} and ϵ_i) were computed during iterations, as shown in Fig. 4. Table 1 contains estimation errors from the last iteration. Although both the greedy and proposed algorithms yield similar error estimations, they differ significantly in their computational requirements and sensor distribution outcomes. On average, the greedy algorithm requires 280 s to be solved, whereas the proposed algorithm finishes in only 6.1 s using a typical PC computer. The obtained sensor location are presented in Fig. 5. In this figure, the first two sensor locations were obtained using greedy algorithms with estimation error measures ϵ_i (Fig. 5a) and ϵ_i^{F} (Fig. 5b). The proposed algorithm produces a unique solution since the sensor selection process does not depend on the estimation error measures ϵ_i nor ϵ_i^{F}. This algorithm yields the sensor distribution shown in Fig. 5c, which includes both inclinometers and accelerometers. The reference response at node 4 (see Fig. 1b) was compared with the reconstructed responses in Fig. 6.

5 CONCLUSIONS

In the contribution, two approaches based on the Kalman filter for optimal sensor placement are presented. For the sake of computational efficiency, a reduced-order model of an actual single-track railway arch bridge is used. The reduced-order model, with few dominant mode shapes, is developed to limit the size of the candidate location set for the sensors (inclinometers and accelerometers) and the response reconstruction set (displacements). As the candidate sensor set comprises sensors of different types, the responses are normalized with

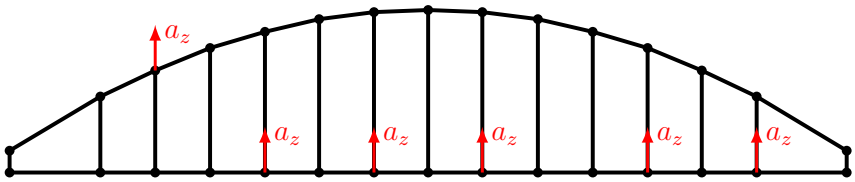

(a) Selected sensors obtained for the greedy algorithm using $\boldsymbol{\epsilon}$.

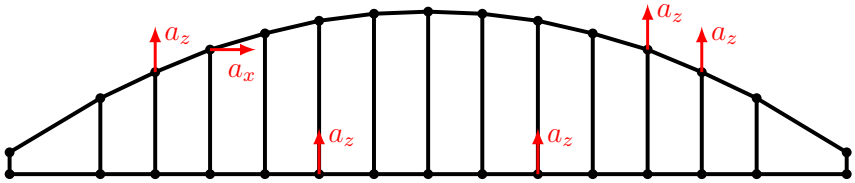

(b) Selected sensors obtained for the greedy algorithm using $\boldsymbol{\epsilon}_i^{\mathrm{F}}$.

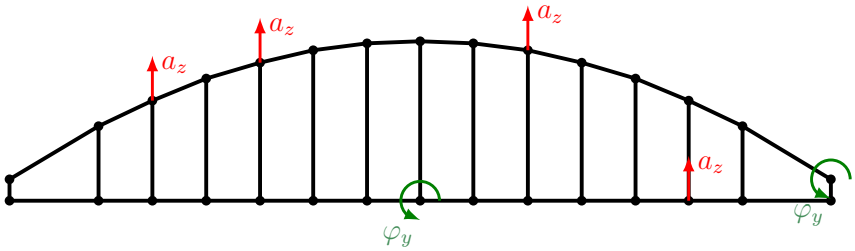

(c) Selected sensors obtained for the proposed algorithm (independent of the estimation error measure).

Figure 5: Determined sensor selection sets for the greedy and proposed algorithms.

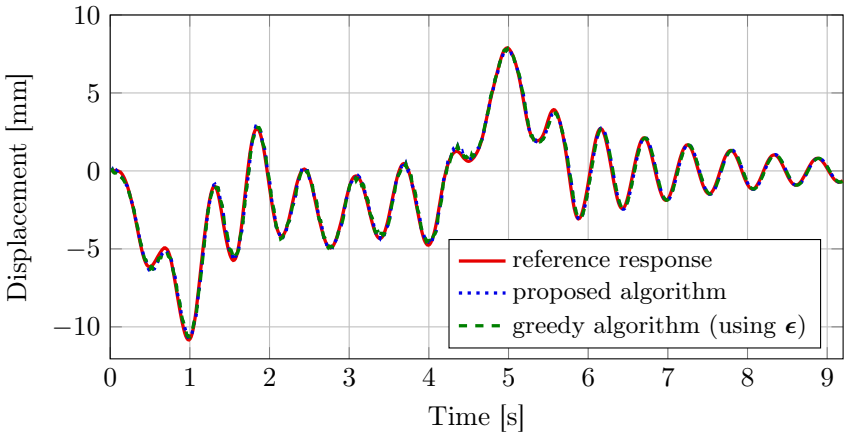

Figure 6: Comparison of the reference vertical displacement (at node 4) with the reconstructed displacements.

respect to the standard deviation of the measurement noise before applying the Kalman filter. The obtained sensor distributions are different for each algorithm; however, in all cases, the reconstructed responses are very close to the reference ones. The important conclusion is the computational effectiveness demonstrated in the investigated example: the proposed algorithm is approximately 45 times faster than the previous greedy algorithm.

ACKNOWLEDGEMENTS

The authors gratefully acknowledge the support of the National Science Centre, Poland, granted under the grant agreement 2018/31/B/ST8/03152.

REFERENCES

[1] P. C. Shah and F. E. Udwadia, "A Methodology for Optimal Sensor Locations for Identification of Dynamic Systems," *Journal of Applied Mechanics*, vol. 45, no. 1, pp. 188–196, 1978.

[2] F. E. Udwadia, "Methodology for Optimum Sensor Locations for Parameter Identification in Dynamic Systems," *Journal of Engineering Mechanics*, vol. 120, no. 2, pp. 368–390, 1994.

[3] P. H. Kirkegaard and R. Brincker, "On the optimal location of sensors for parametric identification of linear structural systems," *Mechanical Systems and Signal Processing*, vol. 8, no. 6, pp. 639–647, 1994.

[4] D. C. Kammer, "Sensor placement for on-orbit modal identification and correlation of large space structures," *Journal of Guidance, Control, and Dynamics*, vol. 14, no. 2, pp. 251–259, 1991.

[5] D. C. Kammer, "Effects of Noise on Sensor Placement for On-Orbit Modal Identification of Large Space Structures," *Journal of Dynamic Systems, Measurement, and Control*, vol. 114, no. 3, pp. 436–443, 1992.

[6] D. S. Li, H. N. Li, and C. P. Fritzen, "The connection between effective independence and modal kinetic energy methods for sensor placement," *Journal of Sound and Vibration*, vol. 305, no. 4-5, pp. 945–955, 2007.

[7] M. I. Friswell and R. Castro-Triguero, "Clustering of Sensor Locations Using the Effective Independence Method," *AIAA Journal*, vol. 53, no. 5, pp. 1388–1391, 2015.

[8] W. Chai, Y. Yang, H. Yu, F. Yang, and Z. Yang, "Optimal sensor placement of bridge structure based on sensitivity-effective independence method," *IET Circuits, Devices & Systems*, vol. 16, no. 2, pp. 125–135, 2021.

[9] B. Błachowski, A. Świercz, M. Ostrowski, P. Tauzowski, P. Olaszek, and Ł. Jankowski, "Convex relaxation for efficient sensor layout optimization in large-scale structures subjected to moving loads," *Computer-Aided Civil and Infrastructure Engineering*, vol. 35, no. 10, pp. 1085–1100, 2020.

[10] C. Papadimitriou, J. L. Beck, and S.-K. Au, "Entropy-Based Optimal Sensor Location for Structural Model Updating," *Journal of Vibration and Control*, vol. 6, no. 5, pp. 781–800, 2000.

[11] C. Papadimitriou, "Optimal sensor placement methodology for parametric identification of structural systems," *Journal of Sound and Vibration*, vol. 278, no. 4-5, pp. 923–947, 2004.

[12] K.-V. Yuen and S.-C. Kuok, "Bayesian Methods for Updating Dynamic Models," *Applied Mechan-*

ics Reviews, vol. 64, no. 1, 2011.

[13] C. Papadimitriou, Y. Haralampidis, and K. Sobczyk, "Optimal experimental design in stochastic structural dynamics," *Probabilistic Engineering Mechanics*, vol. 20, no. 1, pp. 67–78, 2005.

[14] M. Ostrowski, B. Blachowski, G. Mikułowski, and Ł. Jankowski, "Influence of noise in computer-vision-based measurements on parameter identification in structural dynamics," *Sensors*, vol. 23, no. 1, p. 291, 2022.

[15] P. Olaszek, A. Świercz, and F. Boscagli, "The Integration of Two Interferometric Radars for Measuring Dynamic Displacement of Bridges," *Remote Sensing*, vol. 13, no. 18, p. 3668, 2021.

[16] P. Olaszek, I. Wyczałek, D. Sala, M. Kokot, and A. Świercz, "Monitoring of the static and dynamic displacements of railway bridges with the use of inertial sensors," *Sensors*, vol. 20, no. 10, p. 2767, 2020.

[17] R.-P. Hu, Y.-L. Xu, and S. Zhan, "Multi-type sensor placement and response reconstruction for building structures: Experimental investigations," *Earthquake Engineering and Engineering Vibration*, vol. 17, no. 1, pp. 29–46, 2018.

[18] R.-P. Hu, Y.-L. Xu, and X. Zhao, "Optimal multi-type sensor placement for monitoring high-rise buildings under bidirectional long-period ground motions," *Structural Control and Health Monitoring*, vol. 27, no. 6, 2020.